Peer reviewed version

Link to published version (if available):
10.1109/MAP.2017.2731198

Link to publication record in Explore Bristol Research
PDF-document

University of Bristol - Explore Bristol Research
General rights

Design and Validation of a Ultrawideband Measurement Array for Microwave Imaging

David Gibbins, Dallan Byrne,Tommy Henriksson, Beatriz Monsalve, Ian J. Craddock, *Fellow, IEEE*.

Abstract—A compact, enclosed, Ultrawideband (UWB) antenna array is presented to acquire data for a quantitative microwave imaging method. Compared to existing systems, the proposed array allows a directional UWB antenna to be placed close to target object while, at the same time, minimising the volume of the imaging array. The antennas and metallic enclosure are designed to easily integrate with an iterative 3D non-linear inverse scattering technique. The volume of the internal imaging domain has been minimized to reduce computational time spent on reconstructing the dielectrics within the domain. Each cavity-backed element is directional and presents stable transmission characteristics across the 1 to 4 GHz band. The measured antenna characteristics are shown to match well with simulated results across the UWB, when immersed within a lossy dielectric matching liquid. An outlined calibration procedure highlights the straight-forward integration of array measurements with an off-line reconstruction algorithm. Physical measurements of high contrast phantoms are recorded and reconstructions are carried out using a Time-Domain, conjugate-gradient-based, microwave imaging algorithm. The results confirm that the directional antenna array design is well-suited for solving the non-linear inverse problem with measurements recorded over the UWB spectrum.

Index Terms—Microwave Imaging, Inverse Scattering, Ultrawideband, Antenna Array, Time-Domain Imaging.

I. INTRODUCTION

MICROWAVE Imaging is a non-ionizing low-cost method to extract spatial and structural information about dielectric objects within a domain. A transmitting (Tx) antenna element is used to illuminate a target area with an electromagnetic pulse. Diffractive scattering subsequently occurs due to the contrast in permittivity and conductivity at object boundaries within the imaging space. The scattered waves are captured by receiving (Rx) antennas and representative images of the domain are created in post-processing using either radar-based or inverse scattering techniques.

Radar imaging systems provide a qualitative, spatial, scattering map of the dielectric scatterers of the Object-Under-Test (OUT) inside the domain [1]–[3]. Conversely, tomographic or inverse scattering techniques provide structural and spatial information by producing a quantitative map of permittivity and conductivity through solving a non-linear ill-posed inverse scattering problem [4]–[7]. Inverse methods have been shown to resolve targets with a 10% contrast to the background medium at a significant resolution [8]. Frequency hopping techniques can aid in reducing the ill-posedness of the inverse problem. Results from lower frequency reconstructions, with smooth final images due the wavelength constraint, can be used as *a-priori* seeding at higher frequencies to avoid local-

minima convergence and produce finer detail in the dielectric profile of the OUT [9].

The inverse problem is typically solved using iterative gradient-based techniques which minimize the difference between the measured data and a forward model [5], [10]–[13]. The forward model is typically generated using an electromagnetic full-wave solver where the domain must numerically represent the iteratively estimated OUT properties, the surrounding antenna array and system boundary behaviour. This adds considerable constraint on the system design due to the computational overhead involved in simulating detailed antenna architectures and excessive simulation spaces.

A number of previous tomographic studies have reduced this burden by using wire-type antennas which can be easily modelled in full-wave solvers as hertzian dipoles or line sources [14]–[17]. To avoid the limitations of mono-frequency reconstructions, the measurement antenna should capture as much of the desired spectrum as possible. Wire antennas have a wideband response when immersed in appropriate lossy media however, they must be placed at a sufficient electrical distance from the system boundary as their radiation patterns are omni-directional. Undesirable boundary backscatter can introduce model errors into the inverse reconstruction, particularly when the immersion media is low-loss. This increases the size of the forward model simulation domains, adding excessive computational overhead, and in-turn influencing the design of the measurement system which must accommodate the extra space required.

To isolate and minimize the simulation and measurement domain without affecting the quantity of recorded information [18], a number of studies have designed conducting enclosures to surround the array [19]–[23]. To minimise the space further, more recent studies have employed low-profile narrow-band elements, placed directly on the enclosure surface [21], [22]. The patch elements in [22] were extended to resonate at up to four frequencies at the expense of considerable gain loss [23].

In this paper we introduce an UWB microwave imaging measurement system with eight directional elements enclosed within a conducting shell. The design allows for directional UWB antennas to be placed in close proximity to the object in order to acquire data for the inverse scattering problem where:

- Each Large Cavity Backed Wide-Slot (LCBWS) antenna element is designed to have an operational UWB response between 1 and 4 GHz when placed within an appropriate matching medium [24] to record as much data as possible in a single measurement sweep;
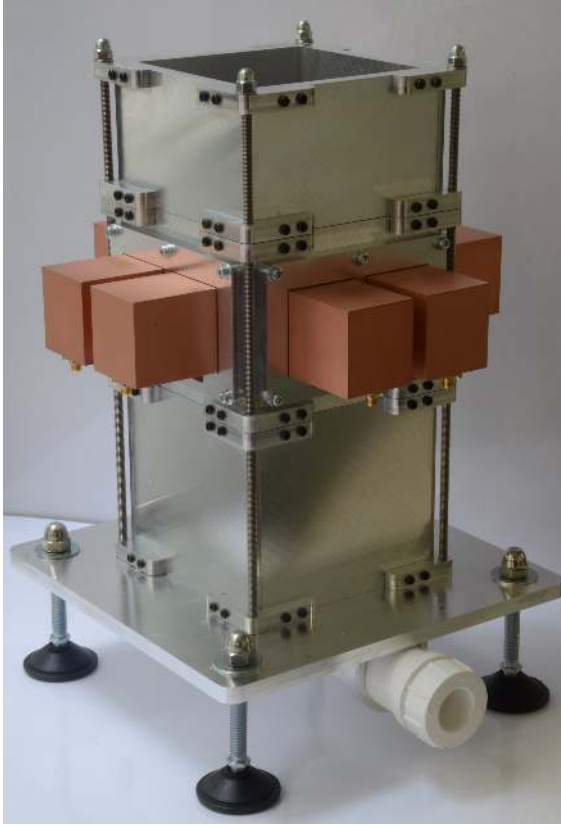
Fig. 1: 8-element imaging array.

Fig. 2: The physical LCBWS antenna shown with a pound coin for scale.

Dimension	a	b	c	d	e	f	g	h	i	j	k
Size (mm)	10.5	57	2	8	12	44	4	14	2.5	40	28

Fig. 3: Detail and dimensions of LCBWS antenna. 1. antenna ground plane, 2. wide-slot aperture, 3. square stub, 4. micro-strip feed line, 5. substrate, 6. air gap between substrate and absorber, 7. absorber.

- The antenna geometry and feed has been designed such that it can be easily and efficiently incorporated within a simulation space. Previous simulated results have shown that the directional array outperforms when compared to an open environment with omnidirectional elements [24];
- The array is contained within a metal enclosure to minimize the size of both the simulation domain and physical space. The magnetic nature of this antenna means that its performance is largely unaffected by the proximity of dielectric objects [24]. The authors believe the dimensions of the presented apparatus, with a volume of $120 \times 120 \times 270$ mm^3, are the smallest of any tomographic measurement array within the literature to date.

The array design is shown in Figure 1 and a single antenna element is illustrated in Figure 2. The array is evaluated with experimental data obtained with phantoms containing a number of high-contrast nylon cylinders. 3D dielectric profiles are produced by solving the inverse problem using the Forward Backwards Time Stepping (FBTS) Time-domain approach [24]–[26] to exploit the entire 3 GHz bandwidth of the acquired scattered fields. A frequency-hopping approach [9], [15], [24], [27] is used to produce quantitative dielectric profiles of two phantoms.

Section II describes the UWB antenna design and details its performance characteristics. The imaging array design is outlined in Section III along with a description of the data acquisition. The FBTS method, experimental phantoms and imaging reconstruction results are illustrated and discussed in Se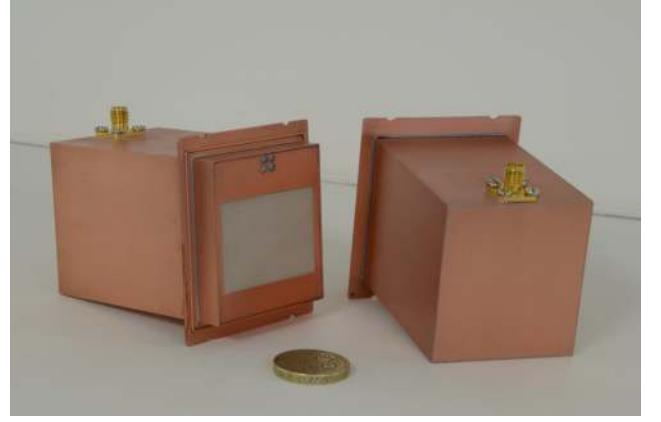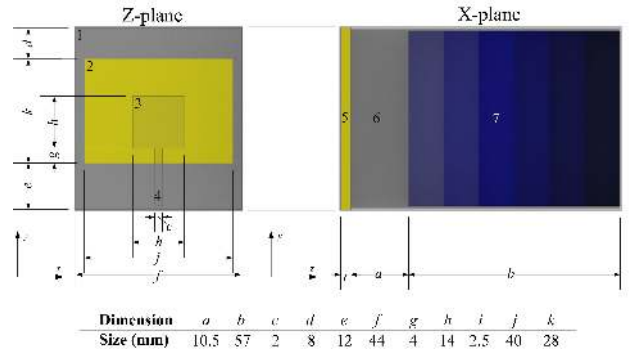ction IV. Section V outlines ongoing research towards the creation of 3D MRI-derived human fore-arm phantoms. Finally, concluding remarks are given in Section VI.

II. DIRECTIONAL UWB LCBWS ANTENNA

The antenna element is the most crucial part of an imaging system, it dictates the range of frequency measurements that may be acquired, the architecture of the system, and most importantly, the reconstructed image quality. The design of the LCBWS antenna (Figure 2) is discussed at the opening of this section before examining its measured and simulated performance characteristics.

A. Antenna Design

The electromagnetic design of this antenna is based on that presented in [24] with some structural modifications, so that the antenna may be manufactured to similar specifications. A detailed image of the antenna design and dimensions are shown in Figure 3. The antenna consists of a rectangular wide-slot aperture located in a rectangular ground plane on the front surface of a 2.5 mm thick RT Duroid 6010 LM (relative permittivity (ϵ_r) = 10.2 at 1 GHz) substrate. The slot is excited by 50 Ω microstrip located on the back surface of the substrate and terminated with a square tuning stub. The large cavity, backing the substrate, is constructed using 1 mm thick copper with flanges to attach it to the array (see section
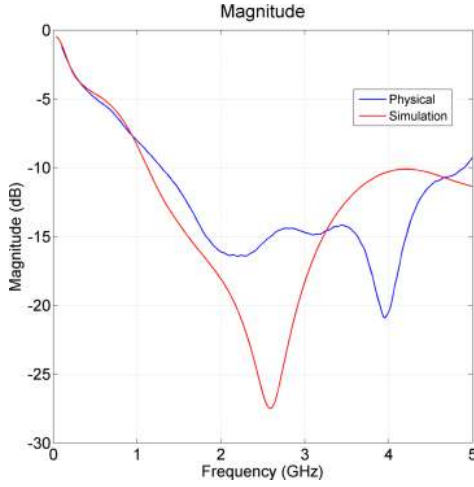
Fig. 4: Measured S11 of the LCBWS antenna within the array and surrounded by matching medium when compared with the simulated S11 in the same environment.

Fig. 5: Simulated and measured S21 of two directly opposing antennas in the array.

III-A). The cavity is filled with a volume of ECCOSORB AN-77 absorber that is spaced 10.5 mm from the back surface of the substrate to ensure that coupling between the absorber and microstrip is minimised. The antenna is fed using a vertical SMP male PCB Receptacle, connected to a length of RG405 coaxial cable and terminated at the exterior of the cavity by a female SMA bulkhead jack.

B. Antenna Performance/Characteristics

Through simulations, performed with an in-house FDTD solver using dispersive algorithms [28], the LCBWS antenna was shown to have good wideband performance in the frequency range 1.2-4 GHz [24]. These characteristics are confirmed by the measured antenna performance. S11 measurements, shown in Figure 4, are recorded when the antenna is located in the imaging array which is filled with a dispersive matching medium [29] with $\epsilon_r = 13.5$ and a static conductivity (σ) of 0.5 S/m at 1 GHz, The -10 dB bandwidth of the antenna is 1.24 GHz to in excess of 4 GHz. This agrees closely with the bandwidth of 1.1 GHz to in excess of 4 GHz obtained when simulating the antenna in the same antenna environment, using a dispersive single pole Debye model for the matching medium. The agreement between simulation and measurement below -10 dB is poor and may be a result of approximations in the simulated feeding arrangement, where the SMP connectors and RG405 cable length are omitted.

The transmission performance of the antenna is shown in Figure 5. This is calculated in the same scenario as the input characteristics, the transmission path being between two antennas directly facing each other across the array. The effects of the RG405 cable are calibrated out in each measurement, to remove their effects and move the measurement plane as close as possible to that in the simulation. Figure 5 shows the transmission characteristics calculated from a physical measurement, a dispersive simulation (in media with similar properties to the measurement matching medium) and a non-dispersive simulation in which a static material model ($\epsilon_r = 13.5, \sigma = 0.5$ S/m) is used to represent the matching
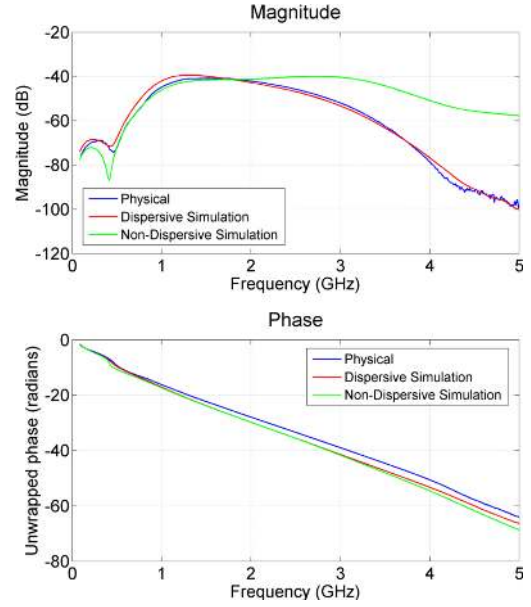
medium. The discrepancies shown illustrate the effects that must be considered when imaging in a dispersive medium. The simulated non-dispersive case demonstrates the performance of the antenna without these effects. The antenna delivers consistent performance across a wide band of frequencies, the magnitude -3 dB bandwidth being 1.15 - 3.4 GHz and the phase linear across all frequencies. By contrast, while the physical measured magnitude is close to the non-dispersive case up to 2GHz, above this point it rapidly diverges, due to the higher frequency dependent loses in the physical matching medium. However, the simulated magnitude with dispersion included shows good agreement with the physical case, which suggests that the antenna model is accurate.

The phase is in good agreement in all three cases in terms of linearity though there is a slight difference in gradient resulting in a π radians difference at 4 GHz equivalent to 10 mm. This is likely due to misalignment of the measurement plane to the simulated model or because of a large permittivity value in the simulated material models.

These results show that the physical element is well suited towards imaging applications within a lossy media. The wideband nature of this antenna allows a large volume of information to be collected while back-radiation from the antenna is minimised, sources of exterior noise are reduced and the power is directed toward the target. The antenna radiation pattern and gain are stable over the required band so present with the same radiation intensity regardless of frequency and the wide beamwidth of the element helps illuminate the target as much as possible.

III. IMAGING ARRAY

Eight replicas of the aforementioned LCBWS antenna were fabricated and embedded within a conductive-enclosure array design, detailed in this section. The data acquisition is documented and a calibration procedure is described to adapt the
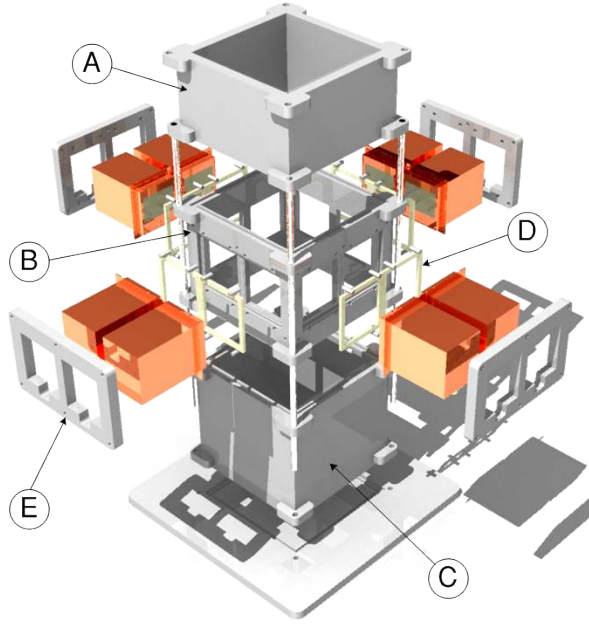
cavity, as pictured in Figure 1. This modular design allows for straightforward array expansion without requiring a complete redesign of the architecture.

Each of the LCBWS elements are housed within the central vertical segment of the array, segment B in Figure 6, with the wide-slot aperture parallel to the internal metallic face. Each element is sealed to the cavity opening using a silicon O-ring which is highlighted by D in Figure 6. A flange, surrounding the body of the LCBWS element, is compressed against the array segment by means of a compression plate, shown as E in Figure 6. The RF connector is located on the underside face of each LCBWS element to avoid unnecessary cable-strain at the feed and to minimise the overall form-factor.

The transmission response of the manufactured elements in the array must be relatively similar to insure uniform imaging response at a number of angles. Figure 7 shows the scattering parameters for a number of Tx-Rx antennas, one group of "Through" channels with antennas directly opposing each other (Figure 7(a)) and another "Diagonal" set with antennas facing in perpendicular directions (Figure 7(b)). There is good agreement between the channels in each set for both the phase and magnitude response between 0.5 and 4 GHz. A small, undesirable discrepancy occurs at 1 GHz in the magnitude response of a single "Diagonal" channel in Figure 7(b). This is most likely an anomaly in the fabrication process where the proximity of the cable feed to the antenna ensures that any minor error in positioning will cause a resonance shift. Such an effect can be mitigated through the calibration process outlined in the following section.

B. Data Acquisition

The antennas are connected to a 20-port Rohde and Shwartz ZNBT VNA via a 1.5 mm semi-rigid coaxial cable. Each port has an independent measurement channel and therefore there is no requirement for an external switching matrix, a common feature in Bristol imaging systems of the past [2], [3]. This ensures isolation between each channel and rapid data acquisition times. Each of the eight Tx elements illuminate the OUT in turn with a single-cycle sinusoid pulse [24] while the other seven Rx elements simultaneously record the scattered fields with a frequency resolution of 501 points and a dynamic range of 120 dB. No monostatic measurements are taken. A full multistatic sweep of 56 channel measurements are recorded in under 5 seconds.

Once the data is recorded, an array calibration step is required to minimise the differences between the physical measurements and the iteratively-updated simulated forward model. The most significant error is due to the discrepancy between the dispersive electromagnetic material properties of the measurement medium and the non-dispersive dielectric model used in the reconstruction process [24]. Other errors can arise due to minor manufacturing errors within the physical array, both material and geometrical, and the inability to physically calibrate out the effects from the antenna cable connector to the aperture.

The calibration method applied is based on the process outlined in [27] and [15]. This technique is well suited for

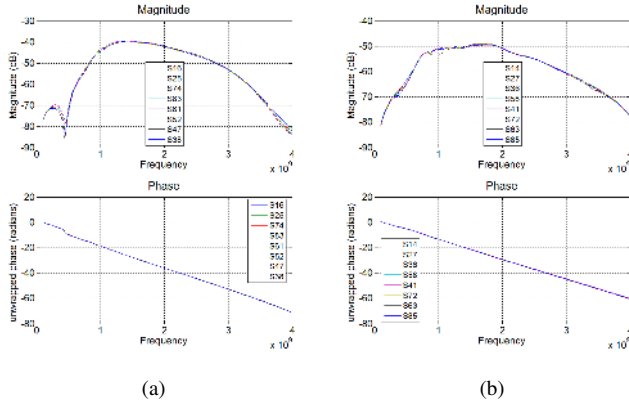Fig. 6: Exploded view of the imaging array.

(a)   (b)

Fig. 7: Transmission response of the (a) "Through" antenna channels and (b) "Diagonal" antenna channels.

measured scatted fields from the system for use in the FBTS inverse scattering scheme.

A. Array Design

A photograph of the metal-enclosed array housing is shown in Figure 1. The eight directional UWB elements can be positioned in close proximity to the OUT, which is placed within a square central array cavity measuring 120 mm x 120 mm x 270 mm. The array has been designed in a modular fashion as shown in the exploded array design model in Figure 6. Three separate segments, highlighted as A, B and C in Figure 6, are stacked vertically and the joints between are sealed with a silicon O-ring. The whole stack is then compressed and sealed using bolted ties, that run the full length of the cavity along the vertical axis, to prevent any leakage when filled with a viscous dielectric matching liquid. The matching liquid can then be removed via a plastic drain that has been installed at the bottom of the main imaging
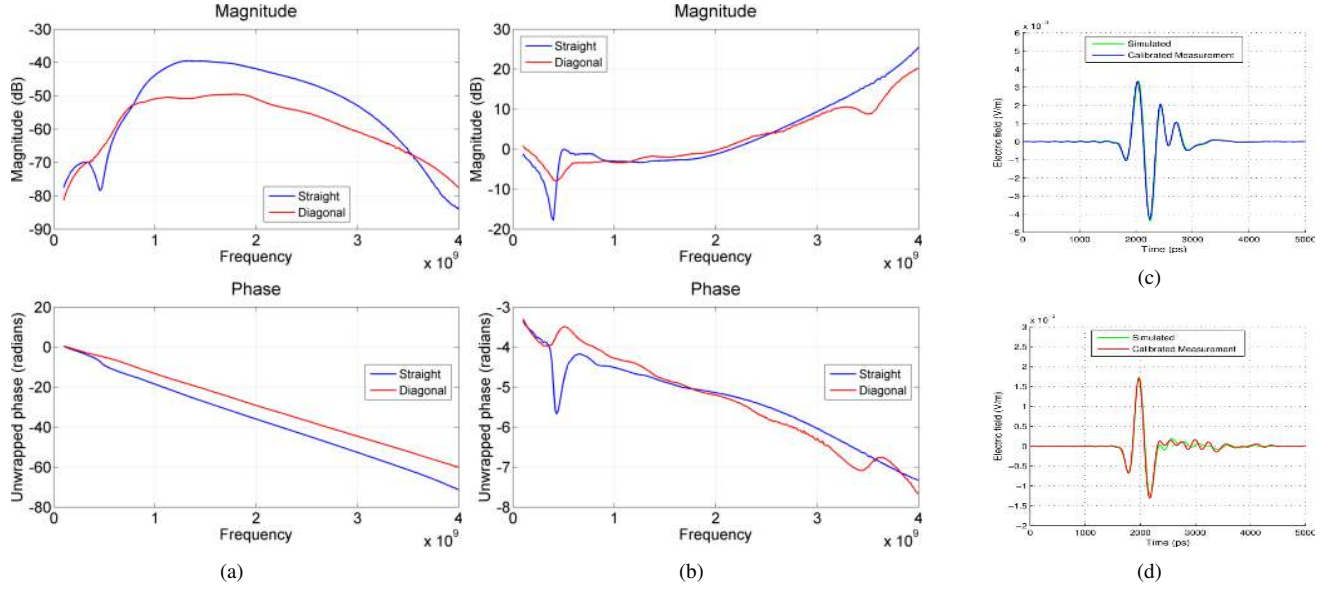
Fig. 8: Calibration process for a "Through" channel (blue) and a "Diagonal" channel (red) with (a) the recorded S-Parameters $\mathbf{E}_P^{data}$ from the VNA and (b) the calibration factor $\mathbf{C}(\omega)$. Signal plots of the calibrated measurement signal $\mathbf{E}_P^{cal}$ as it compares to the output from the EM forward simulator $\mathbf{E}_S^{data}$ for (c) a "Through" channel with directly opposing antenna elements and (d) "Diagonal" channel with perpendicular facing elements.

the proposed imaging system when using a lossy matching medium [27]. The calibrated data is described as

$$\mathbf{E}_P^{cal}(\omega) = \mathbf{E}_P^{data}(\omega)\mathbf{C}(\omega) \qquad (1)$$

where $\mathbf{E}_P^{data}(\omega)$ is the physical measurement data at frequency ω and $\mathbf{C}(\omega)$ is the calibration factor which is denoted as

$$\mathbf{C}(\omega) = \frac{\mathbf{E}_S^{ref}(\omega)}{\mathbf{E}_P^{ref}(\omega)} \qquad (2)$$

with $\mathbf{E}_S^{ref}(\omega)$ is the output from the forward model simulator in a known reference state and $\mathbf{E}_P^{ref}(\omega)$ are measurement data taken within the same reference scenario. The reference scenario involves filling the system solely with a known dielectric medium. The signal can then be converted back into the time domain signal via $\mathbf{E}_P^{cal}(t) = \mathcal{F}^{-1}\{\mathbf{E}_P^{cal}(\omega)\}$.

The S-parameters captured by the VNA $\mathbf{E}_P^{data}$ for a "Through" channel, and "Diagonal" channel, are shown in Figure 8(a). The calibration factor $\mathbf{C}(\omega)$ comparison is illustrated in Figure 8(b) where a number of nulls clearly present which correspond to those of the Tx single-cycle sinusoid input pulse. A measurement and forward simulation are performed with similar imaging scenarios to illustrate the effectiveness of the calibration method. The calibrated measurement signals $\mathbf{E}_P^{cal}(t)$ for the "Through" channel is compared to the simulated signal $\mathbf{E}_S^{data}(t)$ in Figure 8(c) while the comparison for the "Diagonal" channel is shown in Figure 8(d). Both plots highlight the excellent agreement between the simulated and calibrated signals.

IV. IMAGING EVALUATION

The array is designed to image dielectric phantoms using tomographic inverse techniques. Two imaging phantoms with
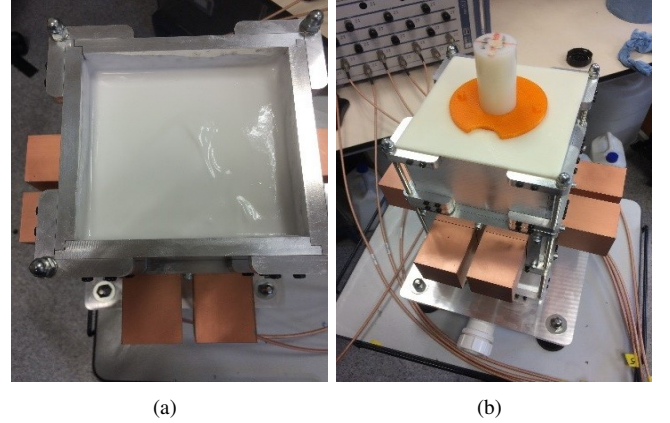

Fig. 9: (a) Array filled with matching liquid. (b) Measurement setup for experiment A with a nylon cylinder at the centre of the system.

cylindrical targets are presented in Section IV-A. A 3D time-domain gradient-based optimisation FBTS algorithm, detailed in Section IV-B, is used to create dielectric profiles of the phantoms. A voxel error metric is outlined in Section IV-C to quantify the results and the final FBTS dielectric reconstructions are presented in Section IV-D.

A. Phantoms

Two nylon cylindrical phantoms are created to assess the imaging algorithm. These rods have a permittivity of 2.2 and conductivity of 0.04 S/m at 1 GHz. The remaining imaging space is filled with a dispersive matching medium with ϵ_r = 13 and σ_r = 0.5 S/m at 1 GHz, created by following the process in [29]. In experiment A, the phantom consists of a single cylinder located at the centre of the array, with a vertical length of 350 mm and a diameter of 32 mm. The phantom for
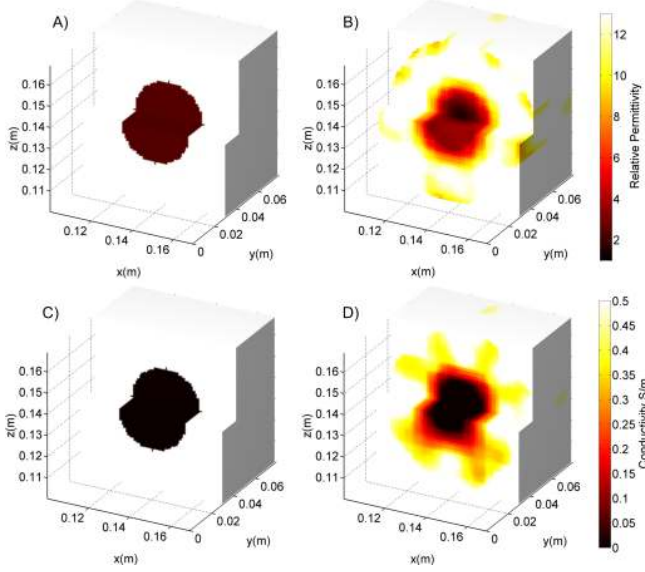
Fig. 10: FBTS Reconstruction of experiment A with a cylinder placed centrally within the array imaging space. The permittivity ground truth is shown in (A) and the reconstruction in (B). The conductivity ground truth result is shown in (C) and the reconstruction shown in (D).
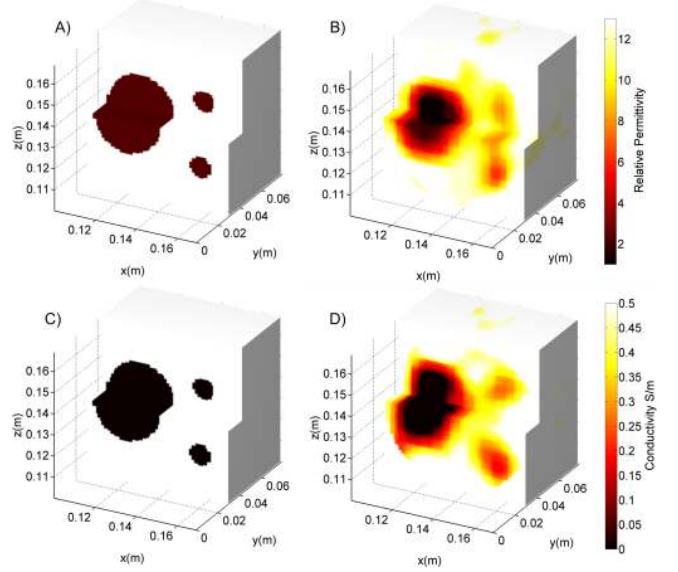

Fig. 11: FBTS Reconstruction of experiment B with cylinder placed off-centre along with two smaller cylinders within the array imaging space. Permittivity (A) GT and (B) reconstruction. Conductivity (C) GT and (D) reconstruction.

experiment B includes this cylinder at an off-centre location, placed beside two narrower cylindrical rods with diameters of 10 mm.

A calibration scan is taken first where the array is completely filled with only the matching liquid as shown in Figure 9(a). This data is used to calculate $\mathbf{C}(\omega)$ in Section III-B. The Ground Truth (GT) for each experiment is illustrated in Figures 10(A), 10(C), 11(A) and 11(C) where the remaining space is filled with matching medium and a machined nylon plate (ϵ_r = 2.2) is used to hold the cylinder in place.

B. Forward Backward Time Stepping Method

The dielectric profiles of the phantoms are created using the Forward Backward Time Stepping (FBTS) technique [24], [25], [30]. Although frequency domain reconstructions are more common within the literature [4], [5], [7], [10], [11], a Time-Domain reconstruction technique is employed to exploit all of the UWB spectrum collected by the LCBWS antenna elements. The FBTS scheme iteratively minimises a cost function to produce a resultant dielectric profile [25]. Further algorithmic detail is provided in [24].

The forward data is generated using a Finite-Difference Time-Domain (FDTD) full-wave EM solver where the antennas and imaging space are modeled in an identical manner to [24]. The entire array is discretised to $227{\times}72{\times}227$ Cartesian grid cells where the smallest cubic cell volume is 0.5 mm^3 and the largest is 1 mm^3. The time step is 0.914 ps, 0.95% of the Courant limit, and 7000 iterations are recorded. No spatial knowledge is included *a-priori* and the forward model imaging domain is initialised with a sole dielectric equivocating to the matching medium described in Section IV-A. The forward model reconstructs static permittivity and conductivity parameters taken at the centre frequency of the input pulse. This

technique has previously been used to successfully reconstruct numerical dispersive tissue-based phantoms [24].

As in [24], a frequency-hopping technique is employed to utilise the available bandwidth and avoid local minima in the cost function. The algorithm begins with a single-cycle sinusoid pulse centred on 1 GHz before switching to a 2 GHz pulse at a particular iteration. A voxel error metric is used to determine when switching will occur.

C. Imaging Metric - Voxel Error

The normalised voxel error between the GT phantom properties and the reconstructed dielectric profiles is calculated at the centre frequency of the input pulse to provide a metric on performance [24], [31]. The metric is defined for permittivity as

$$\delta_i^\epsilon = \frac{\int_\Omega \left| \epsilon^{GT}(\mathbf{r}) - \epsilon_i^{Recon}(\mathbf{r}) \right|^2 dr}{\int_\Omega \left| \epsilon^{GT}(\mathbf{r}) - \epsilon^{BG}(\mathbf{r}) \right|^2 dr} \tag{3}$$

where $\mathbf{r} = (x,y,z)$ is the voxel location, Ω defines the target imaging region, ϵ^{GT} denotes the phantom GT relative permittivity, ϵ_i^{Recon} is the iterative permittivity estimation at iteration i and ϵ^{BG} is the background relative permittivity. Conductivity error is calculated in the same manner and denoted with δ_i^σ.

D. Results and Discussion

Data was collected from the two experimental scenarios and the final reconstruction profiles are presented for experiment A in Figure 10 and experiment B in Figure 11 where GT illustrations are provided on the left-hand side while the reconstructions are on the right. Voxel error metrics are plotted for each experiment in Figure 12 and the convergence rate is shown in Figure 13.

The permittivity and conductivity results reconstruct the dielectric and spatial features quite well in both experiments.
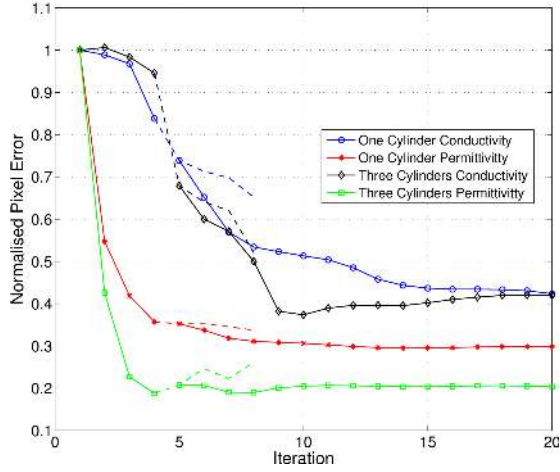
Fig. 12: Voxel error δ metric results for experiments A (One cylinder, Figure 10) and B (Three cylinders, Figure 11). Dashed lines represent the case where the 1 GHz reconstruction continued without a hopping step.

In experiment A, the spatial features are clearly defined in the reconstructions in Figures 10(B) and 10(D). Significant imaging artefacts present outside the target region for both reconstructions but particularly in the case of the permittivity profile in Figure 10(B). These anomalies cause a quantitative mismatch between the GT and reconstructions as shown in the voxel error plot in Figure 12, which shows higher error in permittivity than that of experiment B. These could be removed using spatial regularisation functions which will be applied in future studies.

The more challenging scenario in Experiment B shows a clearly defined large cylinder with less definition for the smaller cylinders in the permittivity profile in Figure 11(B). In contrast, both of the smaller cylinders are well defined in the conductivity profile in Figure 11(D). Again, there are a number of minor artefacts surrounding the targets in the ϵ_r reconstruction in Figure 11(B) but are clearly less pronounced than the single cylinder case in Experiment A. This is confirmed with the voxel error metric result in Figure 12, where experiment B's ϵ_r normalized error converges near 0.2
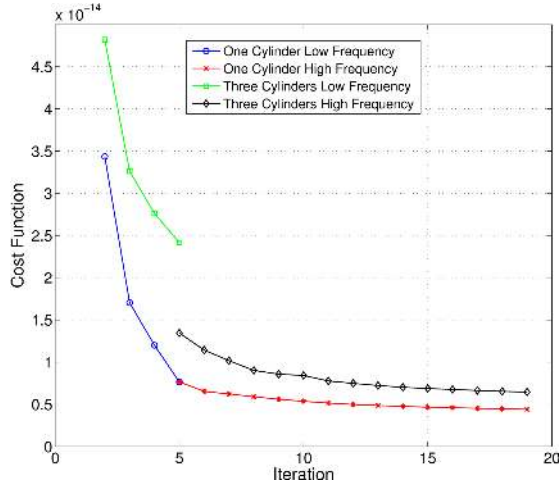

Fig. 13: Cost Function for experiments A (One cylinder) and B (Three cylinders).

after 10 iterations compared to 0.3 for experiment B which suggests that the algorithm is robust when reconstructing more challenging scenarios.

For both experiments A and B in Figure 12, the conductivity profiles are less spatially accurate than those for permittivity. This may arise due to the higher contrast in conductivity (0.5:0.04) between the rods and the matching medium when compared to the permittivity (18:2). This effect is most pronounced for experiment B, where the quantitative conductivity values of the smaller rods are further from the GT than the larger cylinder in Figure 11(D).

Both experiments converge smoothly over 20 iterations in Figure 13 indicating that the target area was reconstructed correctly. The most significant error reduction results from the initial low frequency stage (iteration one to five) for both experiments. Convergence for experiment A shows a smooth transition when the frequency hopping step is applied at the fifth iteration. Once the number of targets increase, as in experiment B, the step to a 2 GHz reconstruction causes the error to be reduced by over 57% at the hop. Improvements from frequency hopping are also evident in Figure 12. The dashed plot lines for permittivity error in experiment A and B highlight how the 1 GHz reconstruction would cause an increase in mismatch, while the error is stabilised after hopping to 2 GHz. Conductivity voxel error results show a less pronounced but similar trend.

As the cost function for each experiment converges in Figure 13, the voxel error in Figure 12 stabilises to a finite value for conductivity and permittivity. The algorithm is more accurate at the central regions than at the upper and lower vertical limits of the array. These regions, at the vertical extremities of the OUT, will present with significant voxel error throughout. There are negligible iterative gradient updates due to the limited EM exposure within these regions as the antenna beampattern tends to primarily illuminate the central portion of the phantom. Although a drawback, the authors highlight the modular design of the array and additional rows of antennas can be easily added if more illumination is required along the vertical axis. This expansion will be addressed in future studies.

V. FUTURE APPLICATION: ARM IMAGING

The results shown in Section IV indicate that the UWB 8-element array shows promise as a Microwave Imaging device and could potentially be used to image biological tissues within the human body. Microwave imaging of the upper and lower limbs have been of recent interest [19], [32], [33] and results have highlighted that the modality could be used for continuous monitoring of fore-arm bone health. To explore this, a number of realistic phantoms must be created prior to any clinical imaging application. This section describes ongoing research to create a number of 3D-printed, MRI-derived, fore-arm phantoms.

The human fore-arm has a significant variety of anatomical features, however the bones (radius and ulna) present with a high vertical symmetry. As a result, an initial 3D-printed fore-arm phantom phantom was created with symmetry along the
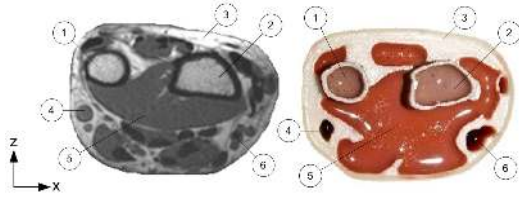
Fig. 14: MRI image (left) and cross-section through arm phantom (right). 1. Ulna; 2. Radius; 3. Adipose (fatty) tissue 4.blood vessel; 5. muscle; 6. Blood vessel.
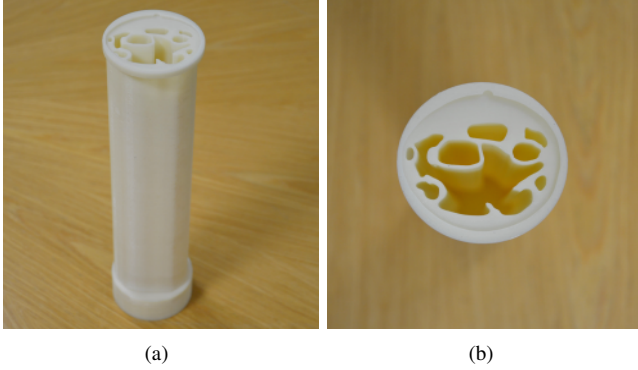

Fig. 15: ABS mould of the fore-arm. (a) 3D view. (b) Top view.

Fig. 16: Different MRI sequences for a female (top) and male (bottom) volunteers. (a)(d) T1-weighted, (b)(e) T2-weighted and (c)(f) positron density.

vertical axis, referred to as the 2.5D phantom herein. Manual segmentation is applied on a cross sectional MRI image taken approximately 50 mm from the wrist, shown in Figure 14 (left), using 3D CAD modelling software (Rhino3D). Four different tissues are manually identified; muscle, bone, adipose (fat) and blood vessels. Tendons, different bone anatomy (cortical bone, cancellous bone and marrow tissue) and cartilages have not been taken into account at this stage. The 2D segmentation is extended along the vertical axis to create the 2.5D model. A number of various support structures and lid have also been created to securely fasten the phantom within the imaging array, similar to those pictured in Figure 9(b).

The full anthropomorphic phantom consists of a plastic mould with compartments for a number of biological tissue-mimicking materials. A 3D-printer with Acrylonitrile Butadiense Styrene (ABS) plastic material has been used to create the mould. The dielectric properties of ABS are found to be at 2 GHz around ϵ_r = 5.3 and σ = 0.08 S/m which can be used to approximate those of adipose tissue.The ABS material is also used as a supporting material for the Ulna and Radius bones. The internal parts of the mould are designed to be filled with tissue-mimicking liquids and a solid skin layer can also be added around the mould's external contour. The phantom is sealed with lacquer prior to adding any tissue materials. Each tissue is represented using a tissue-mimicking liquid, created using the process outlined in [29]. A solid 2 mm skin layer can be created with a Tx-151/H2O mixture [34]. A top view of the fore-arm phantom filled with the different tissues is shown on the right in Figure 14. A 3D and top view of the mould is shown in Figure 15.

The 2.5D design process can be extended to create a number of 3D MRI-derived phantoms. Several MRI scans of the fore-arm of healthy volunteers have been acquired at the University
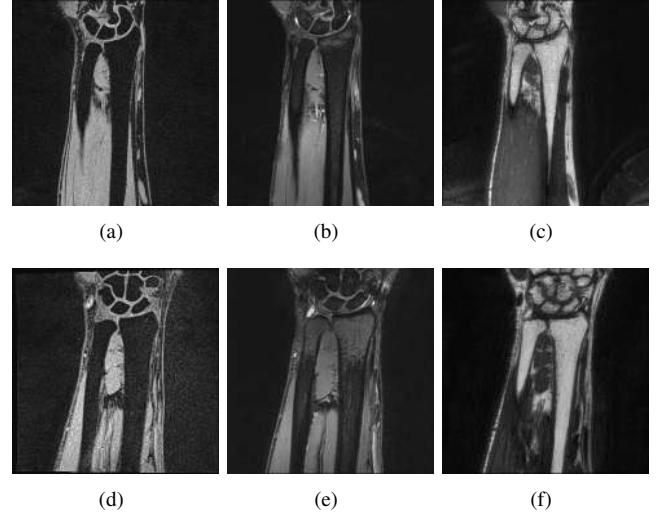
of Bristol's Clinical Research and Imaging Center (CRIC). Volunteers participated under informed consent following a university-approved ethics protocol. Three different 3D sequences (T1-weighted, T2-weighted and proton density) are taken with 0.5 mm isotropic resolution to capture as much data as possible to aid the segmentation process.

Figure 16 shows vertical MRI cross-sectional images from a female and male volunteer within the same age range (both 30-35 years old). The T2-weighted sequences shown in Figures 16(b) and 16(e) highlight the difference between the internal bone structure of each subject. Automatic and semi-automatic segmentation software tools are in development to extract the salient tissue properties of each MRI. Future studies will evaluate the 8-element array with the 2.5D and 3D MRI-derived fore-arm phantoms.

VI. CONCLUSION

An UWB array is proposed to acquire experimental data for an inverse scattering scheme. Eight fabricated UWB antennas can be placed in close proximity to the target. Each magnetic element exhibits solid transmission characteristics between 1 and 4 GHz within a lossy transmission medium and measured reflection/transmission data is shown to match well with the simulated design. The antennas are embedded within a conducting enclosure to minimise the errors encountered when producing forward model data using a numerical full-wave solver. The compact array is designed for simple adaptation in a forward modelling scheme, mitigating excessive simulation space. A calibration scheme is outlined to easily interface the measurement data with an off-line inverse scattering algorithm. A number of cylindrical phantoms were created and reconstructed using a frequency-hopping Forward-Backwards Time-Stepping (FBTS) time-domain approach to the inverse problem. The quality of the reconstructions highlight the array's suitability for microwave imaging problems with dielectric targets. Following this success, ongoing work regarding the

design of human fore-arm phantoms was presented and will be the focus of a forthcoming study.

VII. ACKNOWLEDGEMENTS

REFERENCES

[1] J. M. Sill and E. C. Fear, "Tissue sensing adaptive radar for breast cancer detection-experimental investigation of simple tumor models," *IEEE Transactions on Microwave Theory and Techniques*, vol. 53, no. 11, pp. 3312–3319, 2005.

[2] M. Klemm, J. Leendertz, D. Gibbins, I. Craddock, A. Preece, and R. Benjamin, "Microwave Radar-Based Differential Breast Cancer Imaging: Imaging in Homogeneous Breast Phantoms and Low Contrast Scenarios," *IEEE Transactions on Antennas and Propagation*, vol. 58, no. 7, pp. 2337–2344, 2010. [Online]. Available: http://ieeexplore.ieee.org/ielx5/8/5504492/05452974.pdf

[3] D. Byrne, M. Sarafianou, and I. Craddock, "Compound Radar Approach for Breast Imaging," *IEEE Transactions on Biomedical Engineering*, vol. PP, no. 99, pp. 1–1, 2016. [Online]. Available: http://ieeexplore.ieee.org/stamp/stamp.jsp?tp=&arnumber=7422781

[4] D. K. Ghodgaonkar, O. P. Gandhi, and M. J. Hagmann, "Estimation of complex permittivities of three-dimensional inhomogeneous biological bodies," *IEEE Transactions on Microwave Theory and Techniques*, vol. 31, no. 6, pp. 442–446, Jun 1983.

[5] P. M. Meaney, M. W. Fanning, D. Li, S. P. Poplack, and K. D. Paulsen, "A clinical prototype for active microwave imaging of the breast," *Microwave Theory and Techniques, IEEE Transactions on*, vol. 48, no. 11, pp. 1841–1853, 2000.

[6] S. Y. Semenov, R. H. Svenson, A. E. Bulyshev, A. E. Souvorov, A. G. Nazarov, Y. E. Sizov, V. G. Posukh, A. Pavlovsky, P. N. Repin, A. N. Starostin, B. A. Voinov, M. Taran, G. P. Tatsis, and V. Y. Baranov, "Three-dimensional microwave tomography: initial experimental imaging of animals," *IEEE Transactions on Biomedical Engineering*, vol. 49, no. 1, pp. 55–63, Jan 2002.

[7] A. Abubakar, T. M. Habashy, G. Pan, and M. K. Li, "Application of the multiplicative regularized gauss-newton algorithm for three-dimensional microwave imaging," *IEEE Transactions on Antennas and Propagation*, vol. 60, no. 5, pp. 2431–2441, May 2012.

[8] M. A. Ali and M. Moghaddam, "3d nonlinear super-resolution microwave inversion technique using time-domain data," *IEEE Transactions on Antennas and Propagation*, vol. 58, no. 7, pp. 2327–2336, July 2010.

[9] W. C. Chew and J. H. Lin, "A frequency-hopping approach for microwave imaging of large inhomogeneous bodies," *IEEE Microwave and Guided Wave Letters*, vol. 5, no. 12, pp. 439–441, Dec 1995.

[10] W. Chew and Y. Wang, "Reconstruction of two-dimensional permittivity distribution using the distorted Born iterative method," *IEEE Transactions on Medical Imaging*, vol. 9, no. 2, pp. 218–225, jun 1990. [Online]. Available: http://ieeexplore.ieee.org/ielx1/42/2039/00056334.pdf

[11] N. Joachimowicz, C. Pichot, and J. P. Hugonin, "Inverse scattering: an iterative numerical method for electromagnetic imaging," *Antennas and Propagation, IEEE Transactions on*, vol. 39, no. 12, pp. 1742–1753, dec 1991.

[12] A. Franchois and C. Pichot, "Microwave imaging-complex permittivity reconstruction with a Levenberg-Marquardt method," *IEEE Transactions on Antennas and Propagation*, vol. 45, no. 2, pp. 203–215, feb 1997. [Online]. Available: http://ieeexplore.ieee.org/ielx4/8/12218/00560338.pdf

[13] T. Takenaka, T. Tanaka, H. Harada, and S. He, "FDTD approach to time-domain inverse scattering problem for stratified lossy media," *Microwave and Optical Technology Letters*, vol. 16, no. 5, pp. 292–296, 1997.

[14] P. M. Meaney and K. D. Paulsen, "Nonactive antenna compensation for fixed array microwave imaging Part II-Imaging results," *IEEE Trans. Med. Imag.*, vol. 18, no. 6, pp. 508–518.

[15] A. Fhager, P. Hashemzadeh, and M. Persson, "Reconstruction quality and spectral content of an electromagnetic time-domain inversion algorithm," *IEEE Transactions on Biomedical Engineering*, vol. 53, no. 8, pp. 1594–1604, Aug 2006.

[16] V. Zhurbenko, T. Rubaek, V. Krozer, and P. Meincke, "Design and realisation of a microwave three-dimensional imaging system with application to breast-cancer detection," *Antennas Propagation IET Microwaves*, vol. 4, no. 12, pp. 2200–2211, dec 2010. [Online]. Available: http://ieeexplore.ieee.org/ielx5/4126157/5667224/05667251.pdf

[17] C. Gilmore, A. Zakaria, S. Pistorius, and J. LoVetri, "Microwave imaging of human forearms: pilot study and image enhancement," *International Journal of Biomedical Imaging*, vol. 2013, p. 19, 2013. [Online]. Available: http://dl.acm.org/citation.cfm?id=2537980

[18] L. Crocco and A. Litman, "On embedded microwave imaging systems: retrievable information and design guidelines," *Inverse Problems*, vol. 25, no. 6, p. 065001, 2009. [Online]. Available: http://stacks.iop.org/0266-5611/25/i=6/a=065001

[19] C. Gilmore, A. Zakaria, S. Pistorius, and J. Lovetri, "Microwave imaging of human forearms: pilot study and image enhancement." *International journal of biomedical imaging*, vol. 2013, no. 673027, jan 2013.

[20] C. Gilmore and J. LoVetri, "Enhancement of microwave tomography through the use of electrically conducting enclosures," *Inverse Problems*, vol. 24, no. 3, p. 035008, 2008. [Online]. Available: http://stacks.iop.org/0266-5611/24/i=3/a=035008

[21] M. Haynes, J. Stang, and M. Moghaddam, "Microwave breast imaging system prototype with integrated numerical characterization," *International Journal of Biomedical Imaging*, vol. 2012, 2012.

[22] M. J. Burfeindt, S. Member, N. Behdad, B. D. V. Veen, and S. C. Hagness, "Quantitative Microwave Imaging of Realistic Numerical Breast Phantoms Using an Enclosed Array of Multiband , Miniaturized Patch Antennas," vol. 11, pp. 1626–1629, 2012.

[23] S. M. Aguilar, M. a. Al-Joumayly, M. J. Burfeindt, N. Behdad, and S. C. Hagness, "Multiband miniaturized patch antennas for a compact, shielded microwave breast imaging array," *IEEE Transactions on Antennas and Propagation*, vol. 62, no. 3, pp. 1221–1231, 2014.

[24] D. Gibbins, T. Henriksson, B. Monsalve, D. Byrne, C. Railton, and I. Craddock, "A directional uwb antenna and array for wideband time-domain microwave imaging of biological targets," 2016, *Submitted to: IEEE Transactions on Antennas and Propagation*.

[25] I. Rekanos and A. Räisänen, "Microwave imaging in the time domain of buried multiple scatterers by using an FDTD-based optimization technique," *IEEE Transactions on Magnetics*, vol. 39, no. 3, pp. 1381–1384, may 2003. [Online]. Available: http://ieeexplore.ieee.org/ielx5/20/26972/01198479.pdf

[26] T. Takenaka, H. Zhou, and T. Tanaka, "Inverse scattering for a three-dimensional object in the time domain," *Journal of the Optical Society of America A*, vol. 20, no. 10, p. 1867, 2003. [Online]. Available: https://www.osapublishing.org/josaa/abstract.cfm?uri=josaa-20-10-1867

[27] P. M. Meaney, K. D. Paulsen, and J. T. Chang, "Near-field microwave imaging of biologically-based materials using a monopole transceiver system," *IEEE Transactions on Microwave Theory and Techniques*, vol. 46, no. 1, pp. 31–45, Jan 1998.

[28] D. R. Gibbins, C. J. Railton, I. J. Craddock, and T. N. T. Henriksson, "A numerical study of debye and conductive dispersion in high-dielectric materials using a general ade-fdtd algorithm," *IEEE Transactions on Antennas and Propagation*, vol. 64, no. 6, pp. 2401–2409, June 2016.

[29] T. Henriksson, D. Gibbins, and I. Craddock, "Matching liquid for wideband antenna arrays and microwave imaging systems in biomedical applications," 2016, *In Review: IEEE Antennas and Propagation Letters*.

[30] J. E. Johnson, T. Takenaka, and T. Tanaka, "Two-Dimensional Time-Domain Inverse Scattering for Quantitative Analysis of Breast Composition," *Biomedical Engineering, IEEE Transactions on*, vol. 55, no. 8, pp. 1941–1945, 2008.

[31] A. Fhager, S. K. Padhi, and J. Howard, "3d image reconstruction in microwave tomography using an efficient fdtd model," *IEEE Antennas and Wireless Propagation Letters*, vol. 8, pp. 1353–1356, 2009.

[32] S. Semenov, J. Kellam, Y. Sizov, A. Nazarov, T. Williams, B. Nair, A. Pavlovsky, V. Posukh, and M. Quinn, "Microwave tomography of extremities: 1. dedicated 2d system and physiological signatures," *Physics in Medicine and Biology*, vol. 56, no. 7, March 2011.

[33] P. Meaney, D. Goodwin, A. Golnabi, T. Zhou, M. Pallone, S. Geimer, and K. Paulsen, "Clinical microwave tomographic imaging of the calcaneus: A first-in-human case study of two subjects," *IEEE Transactions on Biomedical Engineering*, vol. 59, no. 12, pp. 3304–3313, Dec 2012.

[34] D. Byrne and I. Craddock, "Time-Domain Wideband Adaptive Beam-forming for Radar Breast Imaging," *IEEE Transactions on Antennas and Propagation*, vol. 63, no. 4, pp. 1725–1735, apr 2015. [Online]. Available: http://ieeexplore.ieee.org/ielx7/8/7080961/07027175.pdf